Efficient computation of past global ocean circulation patterns using continuation in paleobathymetry

Mulder, T. E.; Baatsen, M. L. J.; Wubs, F. W.; Dijkstra, H. A.

Published in:
Ocean modelling

DOI:
10.1016/j.ocemod.2017.05.010

Publication date:
2017

Efficient computation of past global ocean circulation patterns using continuation in paleobathymetry

T.E. Mulder[a], M.L.J. Baatsen[a], F.W. Wubs[b], H.A. Dijkstra[a]

[a]*Institute for Marine and Atmospheric research Utrecht, Department of Physics and Astronomy, Utrecht University, Princetonplein 5, 3584 CC Utrecht, The Netherlands*

[b]*Johann Bernoulli Institute for Mathematics and Computer Science, University of Groningen, P.O. Box 407, 9700 AK Groningen, The Netherlands*

Abstract

In the field of paleoceanographic modeling, the different positioning of Earth's continental configurations is often a major challenge for obtaining equilibrium ocean flow solutions. In this paper, we introduce numerical parameter continuation techniques to compute equilibrium solutions of ocean flows in the geological past, where we change the continental geometry and allow the flow to 'deform' using a homotopy parameter. The methods are illustrated by computing equilibrium three-dimensional global ocean circulation patterns over the last 65 Ma under a highly idealized atmospheric forcing. These results already show interesting major transitions in ocean circulation patterns due to changes in ocean gateways, that may have been relevant for Cenozoic climate transitions. In addition, the techniques are shown to be computationally efficient compared to the established continuation spin-up approach.

Keywords: continuation of fixed points, paleobathymetry, global ocean circulation, past climate transitions

Email addresses: t.e.mulder@uu.nl (T.E. Mulder), m.l.j.baatsen@uu.nl (M.L.J. Baatsen), f.w.wubs@rug.nl (F.W. Wubs), h.a.dijkstra@uu.nl (H.A. Dijkstra)

1. Introduction

Major climate transitions have occurred during the last 65 Ma of Earth's history [1]. One of the most prominent ones was the Eocene-Oligocene Transition (EOT) which happened at about 34 Ma. From oxygen isotope data, it has been deduced that deep sea temperatures decreased by several degrees °C (an isotopic $\delta^{18}O$ signal of 1.2-1.5 ‰) over a period of about 500,000 years [2]. It is generally thought that a crossing of a critical boundary in atmospheric greenhouse gas levels (e.g. pCO_2) was responsible for the EOT and led to the growth of a continental scale ice sheet on Antarctica [3]. However, the fact that the transition appears to consist of two 40,000 year steps separated by a plateau of about 200,000 years [4] suggests that also additional processes have been at work.

Using a highly idealized climate model, Tigchelaar et al. [5] proposed that the first step in the EOT was due to changes in the global ocean circulation, whereas during the second step, land-ice changes occurred. The ocean circulation changes involved a transition between different patterns of the Meridional Overturning Circulation (MOC), and the associated meridional heat transport, due to changes in paleobathymetry. Such transitions are related to the well-known bifurcation behavior of the present-day Atlantic MOC induced by freshwater forcing changes [6]. The study of global ocean circulation patterns versus paleobathymetry is usually done by computing equilibrium patterns for each bathymetry. However, determining such equilibrium patterns is highly computationally demanding as at least a few thousand years of simulation are needed to reach reasonable equilibrium conditions (see e.g., [7]).

An alternative to such transient simulations is the application of continuation methods, where steady states are calculated directly versus parameters. Since the early work of [8], these methods have been applied in many areas of fluid mechanics [9], and more recently also on problems in ocean- and climate dynamics [10, 11, 12]. There are basically two numerical approaches: one is (Jacobian) matrix-based and the other is matrix free. Within the matrix-based techniques, large systems of linear equations have to be solved which requires tailored solvers [13, 14]. In the matrix-free approaches, one only needs the tendency terms of the equations but the schemes often have convergence problems when applied to three-dimensional ocean models [15]. The matrix free techniques may also be used to significantly accelerate spin-up simulations of ocean models [16, 17, 18].

Omta et al. [19] used such a continuation approach to study equilibrium wind-driven ocean circulation patterns within a reduced gravity shallow-water model with several paleobathymetries of the last 65 Ma. They found three major transitions of the surface ocean flow during this period: (i) the appearance of the Antarctic Circumpolar Current in the Oligocene, (ii) the disappearance of the Tethys flow and (iii) the reversal of the Atlantic-Pacific volume transport in the early Miocene. The last transition was shown to be purely geometrically driven involving the relative positions of the different continents. The continuation techniques used by [19] are, however, not suited to determine steady state three-dimensional ocean circulation patterns (e.g. by using the

fully implicit thermohaline circulation model (THCM) in [13]) under a deformation of the bathymetry of the model.

In this paper, we present a novel continuation method to do so; it consists of a predictor followed by a homotopy continuation and is described in Section 2. We apply this method to determine equilibrium flows for 5 Ma intervals during the Cenozoic using paleobathymetries constructed in [20], using highly idealized atmospheric forcing conditions. The results in Section 3 focus on the major changes in volume transports through gateways and the Meridional Overturning Circulation in the different ocean basins. We also present details on the performance of the continuation methodology. A summary and discussion concludes the paper (Section 4).

2. Methods

The methods presented in this paper require an ocean model with a few non-standard capabilities, most importantly the availability of a Jacobian matrix, either explicit or via an action [21]. Spatial discretization of the model equations gives rise to a system of the form

$$B\frac{d\mathbf{x}}{dt} = F(\mathbf{x}, \mathbf{k}), \tag{1}$$

where $\mathbf{x} \in \mathbb{R}^n$ is an n-dimensional state vector, containing unknowns (u, v, w, p, T, S) at each grid point. Bathymetry data is available for each element in the state through the vector $\mathbf{k} \in \{0, 1\}^n$. The dependency on $\mathbf{k}$ is made explicit to stress that bathymetry acts as a parameter in the context of this paper. F is a nonlinear operator $F : \mathbb{R}^n \times \{0, 1\}^n \to \mathbb{R}^n$, arising from the spatial discretization. Fixed points of the model will satisfy $F(\mathbf{x}, \mathbf{k}) = 0$, hence $F(\mathbf{x}, \mathbf{k})$ will be referred to as the residual. It is important to note that the Jacobian matrix J of F with respect to $\mathbf{x}$, given by $J_{ij} = \frac{\partial F_i}{\partial x_j}$, is assumed to be available. $B \in \mathbb{R}^{n\times n}$ is a diagonal matrix determined by the dependencies of the discretization on time derivatives. As B is singular (e.g. due to the discretized continuity equation) the problem (1) is a system of differential-algebraic equations (DAEs).

Bathymetry at the i-th grid point is defined by the land mask

$$k_i = \begin{cases} 1 & \text{land point,} \\ 0 & \text{ocean point.} \end{cases} \tag{2}$$

The land mask affects operators F and J by providing spatial information for the boundary conditions. Moreover, at land points we set $F_i = 0$, $J_{ij} = 0$ for $j \neq i$ and $J_{ii} = 1$, in order to ensure trivial updates in a transient or Newton-Raphson process, reducing the computational effort.

Given a collection of p land masks $\{\mathbf{k}^0, \mathbf{k}^1, \ldots, \mathbf{k}^{p-1}\}$, we aim to traverse a branch of fixed points from one mask to another. That is, find steady states $\mathbf{x}^0, \mathbf{x}^1, \ldots, \mathbf{x}^{p-1}$ such that $F(\mathbf{x}^0, \mathbf{k}^0) = F(\mathbf{x}^1, \mathbf{k}^1) = \ldots = F(\mathbf{x}^{p-1}, \mathbf{k}^{p-1}) = 0$, for gradually changing bathymetries $\mathbf{k}^j$, $j = 0, \ldots, p-1$.

The steady states can be calculated efficiently using a continuation method in the atmospheric forcing, as described in [21], for each paleobathymetry. In a multiple equilibria regime, however, it is not guaranteed that this approach computes fixed points that are located on the same branch. In order to construct a single branch, steady states should be computed using a predictor-corrector-type scheme, which, at its core, is a sequential process. We aim to obtain a new state $\mathbf{x}^j$ at bathymetry $\mathbf{k}^j$ from a previous state $\mathbf{x}^{j-1}$, using only the difference in constraints that arise from different bathymetries, hence without changing the external physical forcing.

In the remainder of this section we will discuss a continuation approach relying heavily on deformations induced by a homotopy constraint of the form

$$G^j(\mathbf{x}, \delta) = (1 - \delta)g(\mathbf{x}) + \delta F(\mathbf{x}, \mathbf{k}^j) = 0, \tag{3}$$

where $\delta \in [0, 1]$ is a continuous homotopy parameter and we require $g(\mathbf{x}) = 0$ to be 'easy' to solve. By construction, a continuation in δ from $\delta = 0$ to $\delta = 1$ computes an estimate of a state satisfying $F(\mathbf{x}, \mathbf{k}^j) = 0$, reaching the desired steady state at $\delta = 1$.

An overview of a single step in the continuation process is given in Figure 1. To proceed from the state-mask pair $(\mathbf{x}^{j-1}, \mathbf{k}^{j-1})$ to $(\mathbf{x}^j, \mathbf{k}^j)$ we first apply a predictor, discussed in Section 2.1. The subsequent computation of deformations induced by the homotopy constraint is explained in Section 2.2.

2.1. Predictor

To make a basic prediction of the new state, we use a map $\mu : \mathbb{R}^n \to \mathbb{R}^n$, based on differences between two successive land masks $\mathbf{k}^{j-1}$ and $\mathbf{k}^j$. The aim of the predictor is to perform adjustments that, without much effort, improve the compatibility of the state $\mathbf{x}^{j-1}$ with the new bathymetry $\mathbf{k}^j$. That is, reduce the residual norm $\left\|F(\mathbf{x}^{j-1}, \mathbf{k}^j)\right\|_2$, which is defined, provided that the state values at land points exist:

$$x_i^{j-1} = \beta, \text{ when } k_i^{j-1} = 1.$$

For our purposes it is convenient to let $\beta = 0$.

The i-th bathymetry difference $d_i^j = k_i^{j-1} - k_i^j$ can either be 1,0, or -1. These values determine the action for our choice of μ as follows

$$\mu_i(\mathbf{x}) = \begin{cases} x_i & \text{if } d_i^j = 0 \text{ (no change)}, \\ 0 & \text{if } d_i^j = -1 \text{ (new land)}, \\ \bar{x}_i & \text{if } d_i^j = 1 \text{ and } i \in I_T \cup I_S \text{ (new ocean)}, \end{cases} \tag{4}$$

where I_T and I_S denote the temperature and salinity indices respectively and $\bar{x}_i$ is the zonal average. In other words, if an ocean point is created we estimate the (absent) tracer values with the zonal average and leave the velocity and pressure values unaltered.

The map μ should, in general, give a significant drop in the j-th residual norm:

$$\left\|F(\mu(\mathbf{x}^{j-1}), \mathbf{k}^j)\right\|_2 \ll \left\|F(\mathbf{x}^{j-1}, \mathbf{k}^j)\right\|_2 . \tag{5}$$

In this way, other adjustments that improve the compatibility of the state-bathymetry pair can be explored as well.

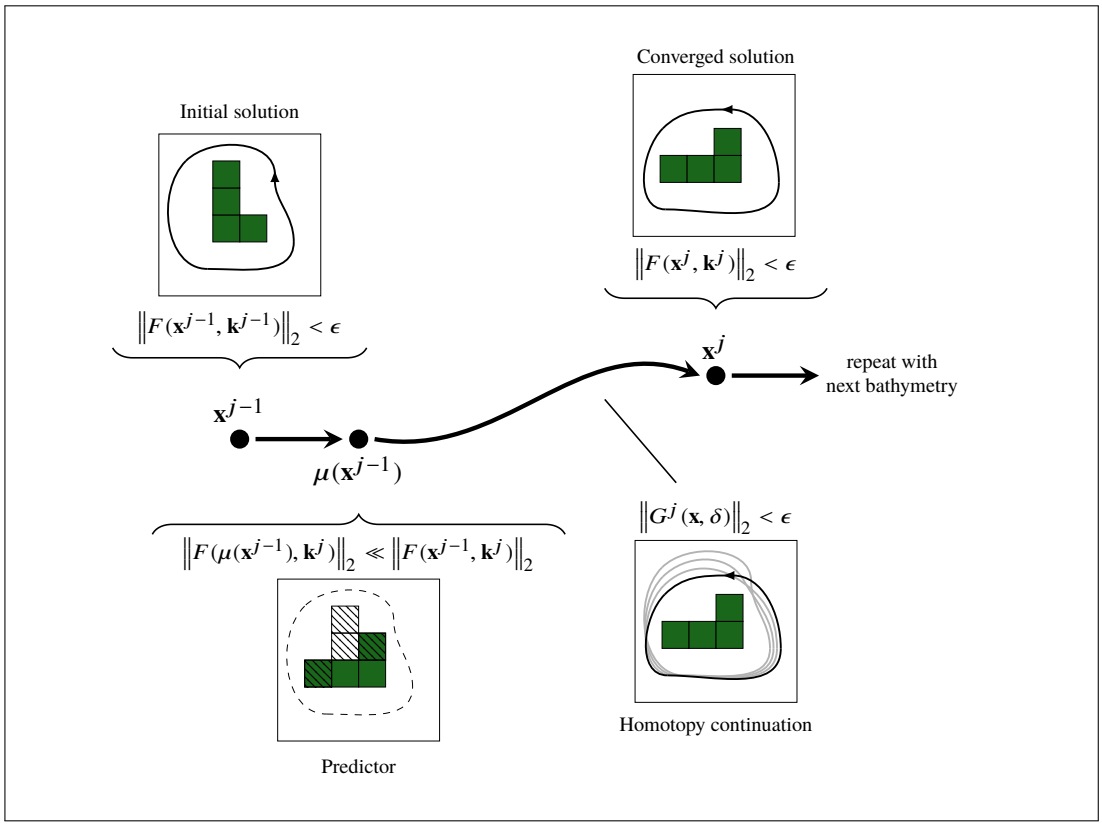

Figure 1: Sketch of a single step in the bathymetry continuation scheme. The starting solution (top left panel) is depicted as a streamline around a topography. Changing to a rotated topography generates new ocean and land points, to which the state is adjusted using the predictor (bottom left). A continuation in the homotopy parameter deforms the predicted solution (bottom right) and converges at a new point on the branch (top right).

2.2. *Homotopy continuation*

Following the predicting phase we begin to compute deformations. Using pseudo-arclength continuation [8] with a homotopy parameter, we traverse a branch of continuous deformations from the predicted state $\mu(\mathbf{x}^{j-1})$ to the state $\mathbf{x}^j$ that satisfies $F(\mathbf{x}^j, k^j) = 0$.

The residual $F(\mathbf{x}, \mathbf{k}^j)$ is embedded [22] in a homotopy constraint based on (3), where we substitute $g(\mathbf{x}) = M(\mathbf{x} - \mu(\mathbf{x}^{j-1}))$ and replace the coefficients involving δ with trigonometric functions:

$$G^j(\mathbf{x}, \delta) = \cos^2\theta\, M\Big(\mathbf{x} - \mu(\mathbf{x}^{j-1})\Big) + \sin^2\theta\, F(\mathbf{x}, \mathbf{k}^j) = 0, \quad \text{with } \theta = \frac{\pi\delta}{2}. \tag{6}$$

The trigonometric functions are used to smooth the transitions between the startup, the interior and the final steps of the continuation. In addition, if the continuation parameter overshoots, that is $\delta > 1$, then the constraints remain well defined.

In equation (6), $M \in \mathbb{R}^{n\times n}$ is a diagonal Boolean matrix, independent of $\mathbf{k}$, with a sparsity pattern similar to that of the mass matrix B in (1): if the i-th row in the system (1) is a differential equation, $M_{ii} = 1$, otherwise $M_{ii} = 0$. By introducing the singular matrix M we maintain the DAE structure of (1). As a result, during the continuation, the state is partly enslaved to its deforming components through the algebraic constraints. The homotopy constraints (6) are, in this way, constructed to mimic an implicit Euler discretization of the original equations.

The nonlinear map $G^j : \mathbb{R}^{n+1} \to \mathbb{R}^n$ depends on a single homotopy parameter δ. To determine states satisfying (6), a solution branch is parameterized with an arclength parameter s: $(\mathbf{x}(s), \delta(s))$. An approximate normalization condition is imposed to close the system:

$$\dot{\mathbf{x}}^T(\mathbf{x} - \mathbf{x}_0) + \dot{\delta}(\delta - \delta_0) - \Delta s = 0,$$

where $(\mathbf{x}_0, \delta_0)$ is a known point on the branch and $(\dot{\mathbf{x}}, \dot{\delta})$ is the tangent at that point with respect to the arclength parameter. Using these tangents the next point on the branch is predicted:

$$\mathbf{x}_1 = \mathbf{x}_0 + \Delta s\, \dot{\mathbf{x}}, \tag{7}$$

$$\delta_1 = \delta_0 + \Delta s\, \dot{\delta}. \tag{8}$$

The predicted point is used as initial guess in a Newton-Raphson iteration to solve the nonlinear system

$$G^j(\mathbf{x}, \delta) = 0, \tag{9}$$

$$\dot{\mathbf{x}}^T(\mathbf{x} - \mathbf{x}_0) + \dot{\delta}(\delta - \delta_0) - \Delta s = 0. \tag{10}$$

Starting at $k = 1$, each step requires the solution of the following bordered system:

$$\begin{bmatrix} \frac{\partial G^j}{\partial \mathbf{x}} & \frac{\partial G^j}{\partial \delta} \\ \dot{\mathbf{x}}^T & \dot{\delta} \end{bmatrix} \begin{bmatrix} \Delta\mathbf{x} \\ \Delta\delta \end{bmatrix} = \begin{bmatrix} -G^j(\mathbf{x}_k, \delta) \\ \Delta s - \dot{\mathbf{x}}^T(\mathbf{x}_k - \mathbf{x}_0) - \dot{\delta}(\delta_k - \delta_0) \end{bmatrix}, \tag{11}$$

where the derivatives of G^j are given by

$$\frac{\partial G^j}{\partial \mathbf{x}} = \cos^2\theta\, M + \sin^2\theta\, J(\mathbf{x}_k, \mathbf{k}^j), \tag{12}$$

$$\frac{\partial G^j}{\partial \delta} = \pi \cos\theta \sin\theta \left[F(\mathbf{x}_k, \mathbf{k}^j) - M\left(\mathbf{x} - \mu(\mathbf{x}^{j-1})\right) \right]. \tag{13}$$

The state and parameter are updated, $\mathbf{x}_{k+1} = \mathbf{x}_k + \Delta\mathbf{x}$, $\delta_{k+1} = \delta_k + \Delta\delta$ and the process is repeated until $\left\| G^j(\mathbf{x}_{k+1}, \delta_{k+1}) \right\|_2 < \epsilon$, for some small tolerance ϵ. To improve convergence we augment the root finding procedure with a line search scheme [23].

Starting at $\delta = 0$, the initial trivial solution is given by $(\mathbf{x}, \delta) = (\mu(\mathbf{x}^{j-1}), 0)$. As we progress, the contribution on the diagonal decreases and the Jacobian matrix J begins to dominate (12). The matrix is ill-conditioned and linear solves with J require

preconditioning, hence we need preconditioning for (12) as well. By incorporating M in the homotopy constraint (6), the sparsity pattern of $\frac{\partial G^j}{\partial \mathbf{x}}$ will equal that of J. A tailored preconditioner for J, described in [13], will then be applicable to the matrix (12) as well. The preconditioner in [13] is based on a block-ILU factorization that exploits the mathematical structure of the primitive equations. Hence, we find that it is essential to achieve a similar structure in (6), in order to apply the tailored preconditioner to (12).

A continuation in bathymetry is achieved with the repeated application of the predictor and the homotopy deformation, where the actual pseudo-arclength continuation occurs at a nested level. The pseudocode in Algorithm 1 summarizes the full scheme.

1: Find $\mathbf{x}^0$ satisfying $\left\|F(\mathbf{x}^0, k^0)\right\|_2 < \epsilon$.

2: **for** $j = 1, 2, \ldots, p-1$ **do**

3: Compute predictor $\mu(\mathbf{x}^{j-1})$ based on difference $\mathbf{k}^j - \mathbf{k}^{j-1}$.

4: Let $G^j(\mathbf{x}, \delta) = \cos^2\theta\ M\left(\mathbf{x} - \mu(\mathbf{x}^{j-1})\right) + \sin^2\theta\ F(\mathbf{x}, \mathbf{k}^j)$.
Perform a pseudo-arclength continuation: $\delta = 0 \rightarrow \delta = 1$.

5: Store $\mathbf{x}^j$ satisfying $\left\|G^j(\mathbf{x}^j, 1)\right\|_2 = \left\|F(\mathbf{x}^j, \mathbf{k}^j)\right\|_2 < \epsilon$

6: **end for**

Algorithm 1: Bathymetry continuation process.

3. Results

We will apply the tools discussed in the previous section to the fully implicit ocean model THCM, described in [13]. THCM is based on the primitive equations with Boussinesq and hydrostatic approximations. The model equations are spatially discretized on a B-grid in the horizontal and a C-grid in the vertical direction, using a second order accurate control volume method. The discretized model is cast in the form we require; it provides a residual $F(\mathbf{x}, \mathbf{k})$, a mass matrix B and a Jacobian J containing explicitly coded differentials of the discrete equations $J_{ij} = \frac{\partial F_i}{\partial x_j}$.

The domain chosen is bounded by longitudes $\phi_E = 0°$, $\phi_W = 360°$ and latitudes $\theta_S = 81°S$, $\theta_N = 81°N$, with periodic boundaries in the zonal direction. The maximum ocean depth is 5000 m. In the horizontal plane we use 120×54 grid points, resulting in a $3° \times 3°$ resolution. In the vertical direction we use 12 levels with grid stretching,

giving a thickness of 95 m in the upper and 786 m in the bottom layer (see next section for details).

To study the sensitivity to topographical changes we prescribe the forcing (wind, buoyancy flux) as a highly idealized zonally-averaged pattern. Such a forcing is a fairly rough approximation of the real forcing (which is poorly constrained and difficult to obtain, even from existing paleoclimate model simulations [7]) but 'correct' to zeroth order. While this forcing will certainly limit the relevance of the results, it serves our primary goal to illustrate the capabilities and performance of the new continuation methodology.

The wind stress consists of only a zonal component varying with latitude, i.e. $\tau(\phi, \theta) = \lambda(\tau_0 \tau^\phi, 0)$, where τ_0 is the amplitude, $\lambda \in [0, 1]$ a continuation parameter and τ^ϕ is given by the analytical profile in [24]. The surface temperature and salinity fields are restored to

$$T_S = T_r + \lambda T_0 \cos\left(\pi \frac{\theta}{\theta_N}\right), \tag{14}$$

$$S_S = S_r + \lambda S_0 \cos\left(\pi \frac{\theta}{\theta_N}\right), \tag{15}$$

with amplitudes T_0, S_0 and reference values T_r, S_r, see Figure 2 and Table 1.

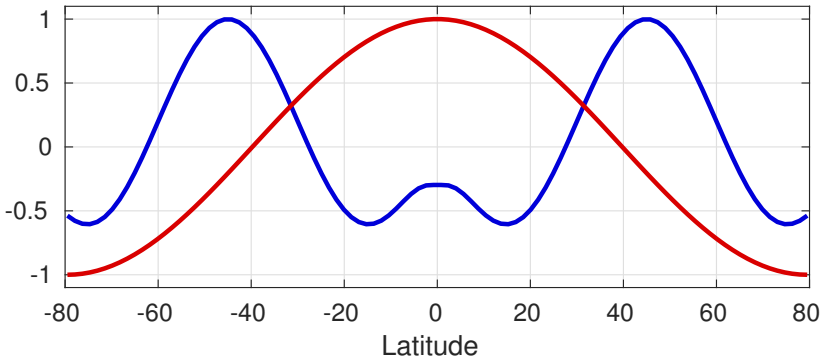

Figure 2: Dimensionless profiles of the surface zonal wind stress τ^ϕ (in blue), surface restoring temperature ($T_S - T_r$) and salinity ($S_S - S_r$) (in red).

T_r	= 15 (°C)	T_0	= 10 (°C)
S_r	= 35 (psu)	S_0	= 1.0 (psu)
τ_0	= 0.1 (Pa)		

Table 1: Values of the forcing parameters in THCM. The other parameters are standard values as in [13].

3.1. Paleobathymetries

A set of bathymetry reconstructions is created for every 5 Ma time frame from 65 Ma to present, using a technique similar to that of [20]. The position of land masses

and continental shelves is based on a plate-tectonic model that uses a paleomagnetic reference framework [25, 26]. Present day topography and coastlines are shifted to their positions at the considered time frame, after which any land topography is removed. The bathymetry of the deep ocean is based on reconstructions by [27] and is adjusted to fit the reference frame used here. The ocean is subsequently updated with shallow plateaus and ridges that are incorporated in the plate-tectonic model.

The above procedure produces a global bathymetry grid at a 0.1° resolution. Each grid cell of THCM thus consists of 30×30 original cells in the horizontal direction, of which the fraction of ocean cells determines the type of the coarse $3^\circ \times 3^\circ$ cell. Vertically, the model contains 12 layers reaching between 0 and $H = 5000$ m depth using a nondimensionalized stretching relation:

$$h(z) = -1 + \frac{\tanh(q_z(z+1))}{\tanh(q_z)}, \tag{16}$$

such that $\tilde{h} = hH$ is the model depth, $\tilde{z} = zH$ is the depth of the equidistant grid and $q_z = 1.8$ the stretching factor. A grid cell is then determined to be ocean when at least 75% of the original cells have a bathymetry value deeper than the depth $\tilde{h}$. This results in a land-ocean mask at the THCM resolution for each of the model levels.

Due to the coarse grid, narrow passages are not resolved and we therefore decided to keep the Tethys seaway 'artificially open' until 25 Ma. To improve the condition number of the Jacobian matrix J, certain grid configurations are discarded as well. Detecting these configurations involves an analysis of the Jacobian matrix, finding unwanted zero diagonals, correcting the corresponding land mask entries and recomputing the matrix. Similar corrections of the land mask can be achieved by inspecting the residual. Finally, to reduce computing time we discard inland seas and parts of the Arctic Ocean that are only connected to the global ocean through shallow overflows.

3.2. Initial tangent

First, a continuation spin-up (note that no time stepping is used) is performed for a bathymetry ($\mathbf{k}^0$ in Section 2) at 65 Ma, using a parameter continuation in forcing from $\lambda = 0$ (zero solution) to $\lambda = 1$ (full equilibrium). The computed steady state is referred to as $\mathbf{x}^0$. Subsequent states for bathymetries at 60 Ma, 55 Ma, 50 Ma, ..., 20 Ma are computed using the bathymetry continuation approach (as in Algorithm 1).

In a pseudo-arclength continuation, the predictor equations (7)-(8) require tangents with respect to the arclength parameter $(\dot{\mathbf{x}}, \dot{\delta})$. At initialization, these tangents cannot be found using finite differences. Instead, assuming $\dot{\delta} = 1$ at $s = 0$ and using $\frac{d}{ds} G^j(\mathbf{x}(s), \delta(s)) = 0$ the tangent $\dot{\mathbf{x}}$ can be found by solving

$$\frac{\partial G^j}{\partial \mathbf{x}} \dot{\mathbf{x}} = -\frac{\partial G^j}{\partial \delta}. \tag{17}$$

Substituting the starting point $\mathbf{x}_0 = \mu(\mathbf{x}^{j-1})$, $\delta_0 = 0$ in (12)-(13), we find $\frac{\partial G^j}{\partial \mathbf{x}} = M$ and $\frac{\partial G^j}{\partial \delta} = 0$. In practice, however, the derivative $\frac{\partial G^j}{\partial \delta}$ is calculated using a finite

difference, which, at the starting point gives

$$\frac{G^j(\mathbf{x}, \delta+\eta) - G^j(\mathbf{x}, \delta)}{\eta} \approx \frac{1}{\eta}\left[(\theta+\eta)^2 - \theta^2\right] F(\mu(\mathbf{x}^{j-1}), \mathbf{k}^j)$$
$$= \eta F(\mu(\mathbf{x}^{j-1}), \mathbf{k}^j).$$

The initial state tangent is obtained from

$$M\dot{\mathbf{x}} = -\eta F(\mu(\mathbf{x}^{j-1}), \mathbf{k}^j). \tag{18}$$

Restricting M to its non-singular part, we find that the state tangent vector corresponding to the deforming components is given by the initial residual.

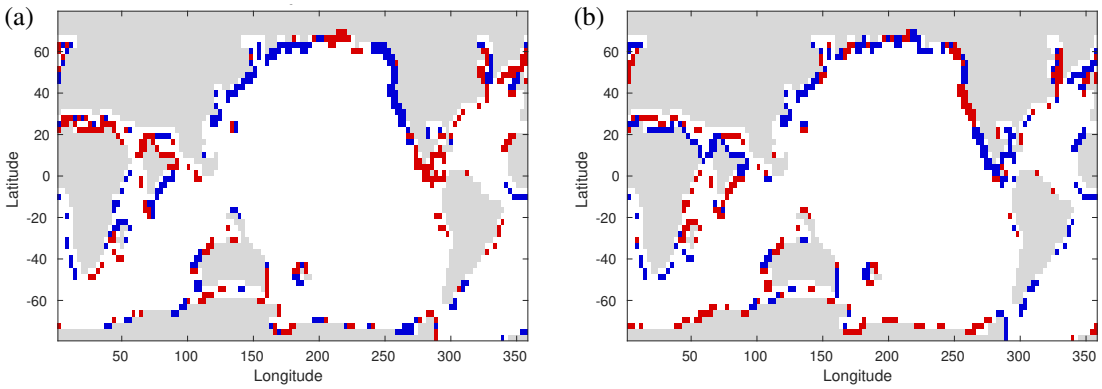

Figure 3: Surface (a) zonal and (b) meridional velocity deficiencies given by the initial tangent in the homotopy continuation process from 50 Ma to 45 Ma. The signs of significant contributions are labelled red (positive) and blue (negative).

For one particular case (50Ma $\rightarrow$ 40 Ma), the horizontal surface velocities of the initial state tangent $\dot{\mathbf{x}}$ are shown in Figure 3, where significant positive and negative contributions are labelled red and blue, respectively. For these surface points we see that major changes take place at the continental margins as these are the regions where many land points are removed and introduced. Entering the incompatible state $\mu(\mathbf{x}^{j-1})$ in the constraints $F(\cdot, \mathbf{k}^j)$ returns deficiencies for every unknown. By negating the list of deficiencies a tangent is created that allows the first prediction of the state in the direction of gradual deformations induced by $G^j(\mathbf{x}, \delta) = 0$.

3.3. Major ocean flow changes

The patterns of the global barotropic stream function at 60 Ma, 50 Ma, . . . , 20 Ma obtained by the bathymetry continuation are plotted in Figure 4, together with volume transports (in Sv, 1 Sv = 10^6 m^3s^{-1}) through the major gateways (see caption for acronyms). Overall, there is much similarity with these patterns and those computed with a shallow-water model [19], where an atmosphere model-based Cretaceous wind-stress pattern was used as prescribed forcing. Although the wind-stress forcing is

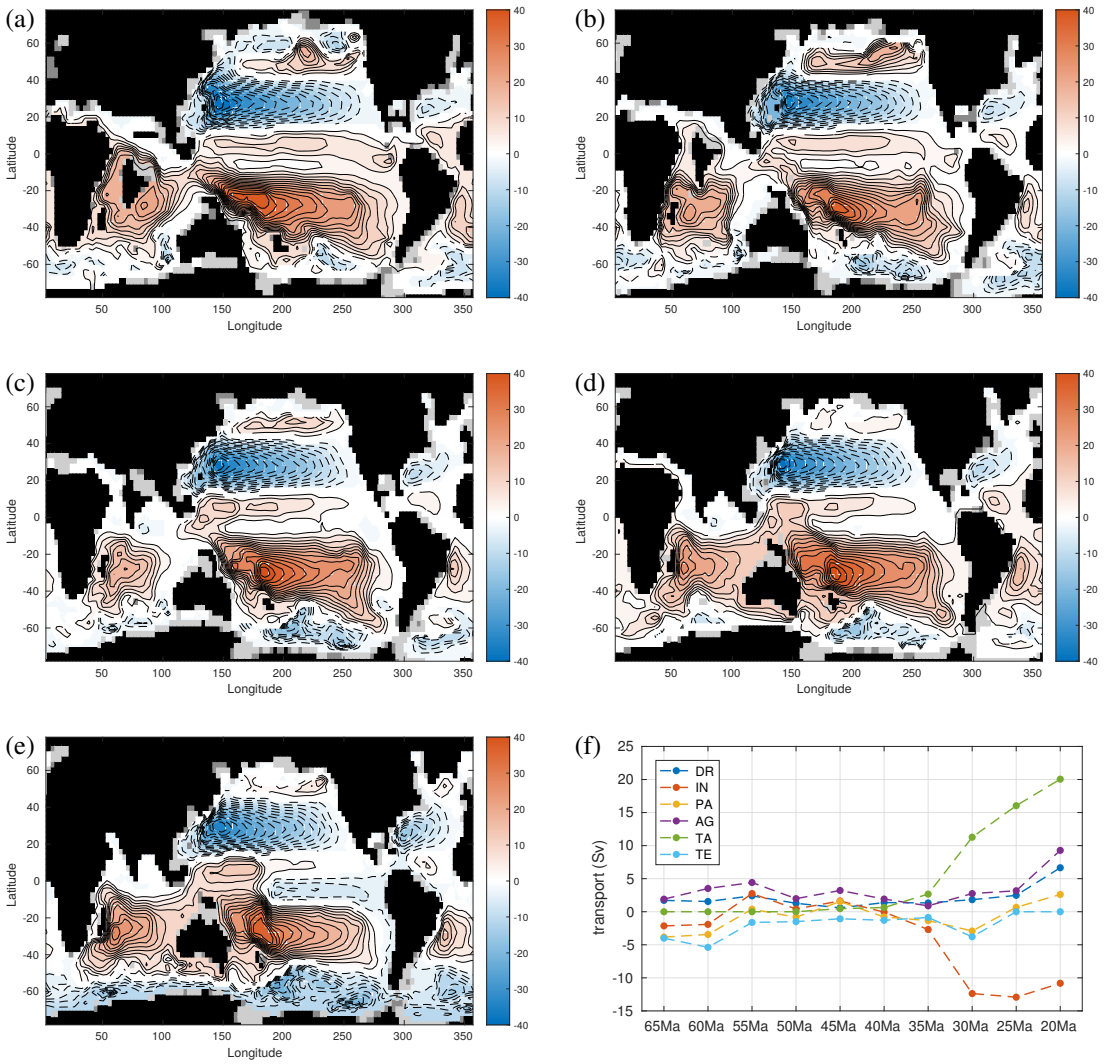

Figure 4: Steady state barotropic stream function patterns for the global ocean model (THCM) configuration with bathymetries at (a) 60 Ma, (b) 50 Ma, (c) 40 Ma, (d) 30 Ma and (e) 20 Ma. The first steady state is calculated with a continuation in forcing using a bathymetry for 65 Ma. The states at 60 Ma and onwards are found using the bathymetry continuation procedure in Algorithm 1. (f) Volume transports are calculated at the Drake passage (DR), Indonesian throughflow (IN), Panama Straits (PA), Agulhas (AG), Tasman (TA) and Tethys (TE) gateways. A grayscale is used to illustrate the bathymetry, with lighter shades at increasing depth.

highly idealized here, the gyres and western boundary currents in each of the basins are captured by the model. The width of the Atlantic basin is relatively small and hence current velocities are much weaker than in the Pacific. As in [19], a circum-India current is found here in the 60 Ma paleobathymetry which disappears between 50 Ma and 40 Ma because of the India-Eurasia collision.

All gateway transports are relatively small between 65 Ma and 35 Ma; note that they

are smaller as in [19] because here many of the gateways are much shallower than the layer depth used in [19] for the computation of the transports. Notable increases and changes in gateway transports occur during the period between 40 Ma and 30 Ma. Due to the separation of Australia from Antarctica, transport through the Tasman gateway (TA) increases, most of which is returned through the Indonesian Throughflow (IN). The widening of the Drake passage results in a weak Antarctic Circumpolar Current (ACC) at 30 Ma. Until the Tethys gateway (TE) is closed at 25 Ma the transport through the Panama Straits (PA) is closely linked to the transport through the Tethys. At 25 Ma a flow reversal has occurred between the Atlantic and Pacific, similar to the results in [19] and [28].

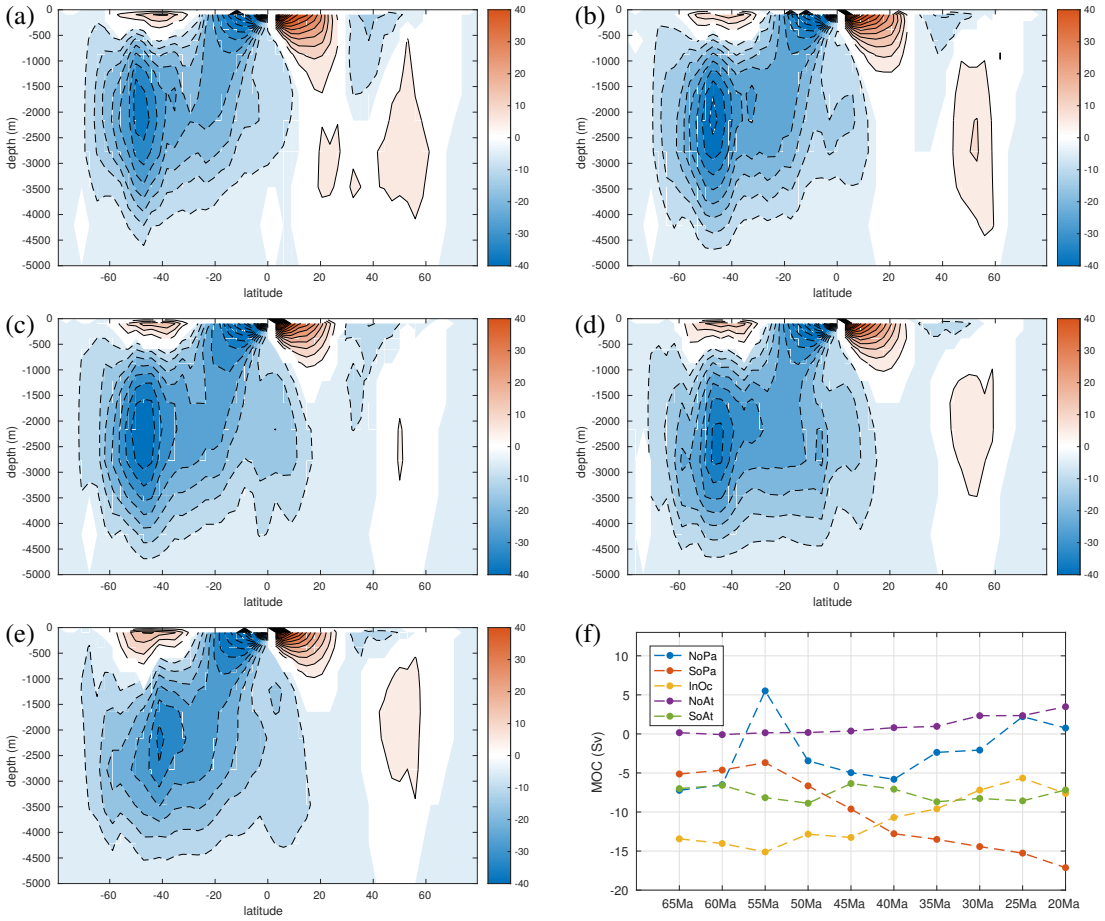

Figure 5: Steady state patterns of the global MOC stream function for a global ocean configuration with bathymetries at (a) 60 Ma, (b) 50 Ma, (c) 40 Ma, (d) 30 Ma and (e) 20 Ma. The first steady state is found with a continuation in forcing at 65 Ma. The states at 60 Ma and onwards are found using the bathymetry continuation procedure in Algorithm 1. (f) Meridional overturning stream function extrema below 1000 m and at fixed latitudes (38N, 38S) are plotted for the North Pacific (NoPa), South Pacific (SoPa), Indian Ocean (InOC), North Atlantic (NoAt) and South Atlantic (SoAt).

The patterns of the global meridional overturning stream function at 60 Ma, 50

Ma, ..., 20 Ma are plotted in Figure 5, together with extrema below 1000 m of the overturning in the major basins (see acronyms in the caption of the figure). Because of the restoring boundary conditions for temperature and salinity, the resulting MOC is affected only by the prescribed surface density field. Here, the north-south asymmetry in the continental distribution favors a southern sinking state (with highest amplitude in the southern part of the basin). Over the period 65 Ma to 20 Ma the patterns of the MOC do not change much (because of the restoring boundary conditions). In the North Atlantic (NoAt in Figure 5f) deep water formation emerges as the basin widens and the MOC transport increases. In the South Pacific (SoPa in Figure 5f), the southern sinking cell strengthens over the geological evolution towards the present-day.

3.4. Performance

To illustrate the performance of the methodology (within THCM) we show results for several 5 Ma period continuations. In addition, we compare the computational effort of the bathymetry continuation with that of a continuation spin-up (by using the forcing parameter λ), as described in [21].

First we investigate the performance of the predictor step. We inspect the j-th residual norm $\left\|F(\cdot, \mathbf{k}^j)\right\|_2$ before and after applying the predictor, see Table 2. Here we use the approach discussed in Section 2.1, where we substitute unknown tracer values with their zonal average. The effect of this simple adjustment is clear; a substantial reduction occurs, especially when the number of substitutions is high. Hence replacing the tracers gives a significantly improved starting point for the homotopy continuation. The improvements appear to diminish when the number of new ocean points decreases. Note, however, that this does not imply a reduction in difficulty of the corresponding 5 Ma continuation step. Small changes in bathymetry might still give large shifts in circulation patterns.

Step	$\left\|F(\mathbf{x}^{j-1}, \mathbf{k}^j)\right\|_2$	$\left\|F(\mu(\mathbf{x}^{j-1}), \mathbf{k}^j)\right\|_2$	Factor	New ocean	New land
50 Ma to 45 Ma	9.685×10^5	5.032×10^4	19.25	2347	2577
45 Ma to 40 Ma	9.672×10^5	5.027×10^4	19.24	2190	2457
40 Ma to 35 Ma	7.183×10^5	7.659×10^4	9.38	1684	1547
35 Ma to 30 Ma	8.951×10^5	1.901×10^5	4.71	1786	1747

Table 2: Performance of the predictor discussed in Section 2.1: norms of the j-th residual and the improvement factor. The number of new land and ocean points are included as well.

As the chosen scheme is quite straightforward, it would appear that the predictor can be improved using more sophisticated adjustments. One could, for instance, attempt to solve a small projected problem involving new ocean points and their neighbors. Another option might be to perform several time steps; letting empty ocean points become more physical through a natural time evolution.

Next, we investigate the performance of the homotopy continuation. In Figure 6a the evolution of the j-th residual norm is plotted against the number of continuation

steps. Substantial progress is made during the startup phase, where the continuation process moves onto the branch of deformations using the initial tangent discussed in Section 3.2. In the interior of the homotopy continuation a steady decline of the residue is visible. Then, as the continuation passes $\delta = 0.8$, the Newton iterations become computationally expensive (see Figure 6b). In the final phase of the continuation some overshoots ($\delta > 1$) occur, which are visible as a plateau or an increase in the convergence plot. This is due to the fact that we solve $G^j(\mathbf{x}, \delta) = 0$, which is only equivalent to $F(\mathbf{x}, \mathbf{k}^j) = 0$ at exactly $\delta = 1$. When the continuation moves beyond $\delta = 1$ a secant procedure ensures convergence at $\delta = 1$. Hence, the total convergence of the bathymetry continuation is robust.

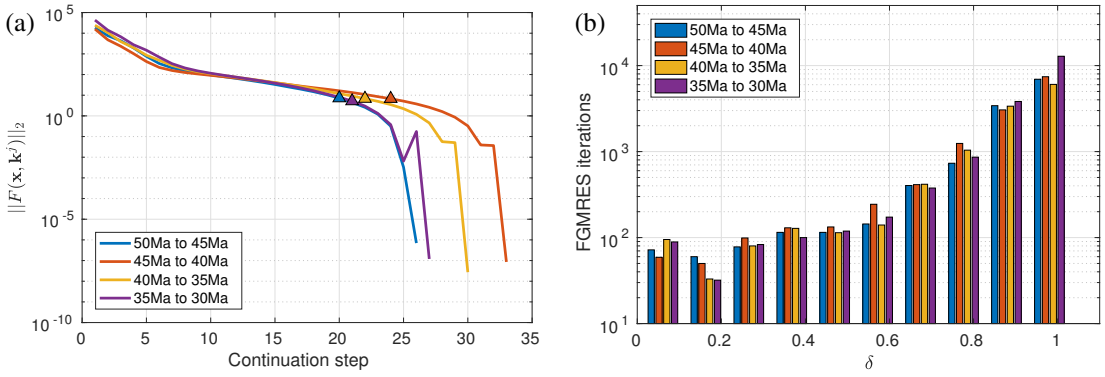

Figure 6: (a) Convergence behavior for different steps in the bathymetry continuation. Triangles denote the first point beyond $\delta = 0.8$. (b) Total number of FGMRES iterations spread over 10 equidistant bins in the homotopy parameter δ. Each bin resembles a varying amount of linear solves due to the adaptive continuation steps.

In Figure 6b the total number of linear FGMRES [29] iterations inside the Newton solver are grouped into 10 equidistant parameter ranges. This allows an overview of the required work at different stages of the continuation, without neglecting adjustments in the continuation step size. In the start-up phase of the homotopy continuation there is some effort associated with the small step size that is needed to get onto the branch of deformations. The next parameter range shows significantly less linear solves. As the continuation progresses the total effort increases, reaching its peak in the final converging phase. Note that in the interior of the continuation, between $\delta = 0.2$ and $\delta = 0.8$, the effort remains relatively modest, which is advantageous as we will see next.

In order to indicate the computational cost of the bathymetry continuation we compare individual 5 Ma steps to independent continuation spin-ups (in the parameter λ) at the destination bathymetries. All common parameters, such as the solver and preconditioner settings and tolerance values, in different components of the continuation algorithm are kept equal. Experiments are performed using 24 cores within a single node of the Dutch supercomputing facility Cartesius at SURFsara in Amsterdam (www.surfsara.nl).

Step	Homotopy continuation	Spin-up
50 Ma to 45 Ma	02:05:36	05:57:29
45 Ma to 40 Ma	02:08:36	05:41:51
40 Ma to 35 Ma	01:51:48	04:52:27
35 Ma to 30 Ma	02:48:33	04:40:52

Table 3: Computing times (hh:mm:ss) to reach the steady state.

From the runtimes we see that the bathymetry continuation is reasonably competitive in the studied cases, although a major overshoot in the step from 35 Ma to 30 Ma is clearly visible in the timing results. To reveal why the continuation spin-ups perform worse, we again inspect the total number of FGMRES iterations for 10 bins in the combined forcing parameter λ, see Figure 7.

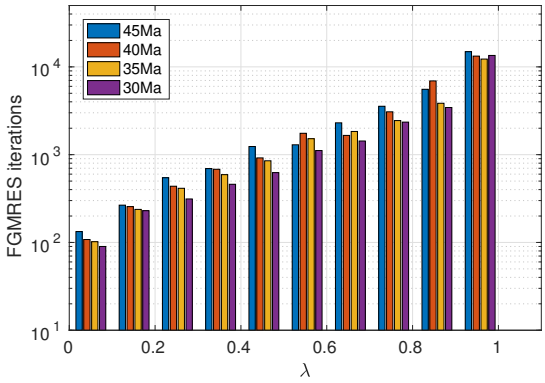

Figure 7: Total number of FGMRES iterations in 10 equidistant bins in the combined forcing parameter λ for continuation spin-ups at different bathymetries.

Comparing Figure 7 with Figure 6b, we find that the increase in effort during a continuation spin-up is immediate, whereas it is postponed in the bathymetry continuation. This can be partly related to the contribution of M in the Jacobian matrix $\frac{\partial G^j}{\partial \mathbf{x}}$, which enhances the Jacobian's posedness for most of the continuation, but also to the fact that a pre-existing solution is adapted; that is, the solution is not build from scratch as in the continuation spin-up. Note, also, that the continuation parameter δ is embedded in trigonometric functions, which spread the amount of work towards the interior of the continuation. Without this adjustment the difference between Figures 7 and 6b would be even more expressed.

4. Summary and Discussion

We have presented a novel continuation approach to compute branches of steady three-dimensional ocean circulation patterns versus a change in continental geometry and bathymetry. The method relies on the predictor-homotopy approach as described in Section 2 and it is the first of its kind where changes in flow domain can be incorporated

efficiently. So far, only the two-step residue continuation approach was available to tackle these problems but this procedure often did not work for changes in flow domain [12, 30].

The bathymetry continuation allows an efficient computation of ocean circulation patterns in the geological past since it circumvents the long spin-up procedure (of a few thousand years of time stepping) which is needed in traditional approaches. The results shown here in Section 3 are still for a relatively low resolution ($3^\circ \times 3^\circ$ in the horizontal and 12 vertical levels) global ocean model (THCM as described in [13]) and for highly idealized (zonally averaged restoring) boundary conditions that remain fixed throughout the changing land configurations.

The vertically averaged circulation (barotropic stream function) shows the major transitions in currents and gateway transports, which were already found in [19] in a shallow-water model. In particular, the Atlantic-Pacific flow reversal at about 25 Ma [31] is already captured under these idealized boundary conditions and hence appears to be a very robust feature. The Meridional Overturning Circulation does not show much variation over the period 65 Ma to 20 Ma, but this is due to the imposed restoring boundary conditions for temperature and salinity. Once mixed boundary conditions are used, one expects many more changes over the geological period and maybe the occurrence of multiple equilibria [6, 32].

There is no principal problem to extend the THCM [13] towards a paleoclimate model, including (land and sea) ice, an atmosphere energy balance model and a land-surface model and efforts are currently underway to develop such a model. The resulting coupled model will allow the continuation methodology described in this paper, without having the limitations imposed by the idealized atmospheric forcing. The parallel preconditioning techniques needed to solve the linear systems within the Newton-Raphson methods [14] are also in a stage that horizontal resolutions of 1° can be handled.

Such models will be useful to investigate the role of the multiple equilibrium flows in the ocean in past climate transitions, such as possibly the EOT [5]. They can also be helpful to investigate the sensitivity of equilibrium climate states due to changes in bathymetry, the latter still being quite uncertain for large periods over the last 65 Ma [20]. In particular, the ocean circulation changes due to uncertainties in the reconstructions can be efficiently addressed.

We expect that the bathymetry continuation is sufficiently general to be applied to the continuation of periodic orbits, which requires constraints that incorporate the flow of the model [33]. Such a continuation would require a similar homotopy-based deformation with a suitable embedding of the constraints that determine periodic orbits. The construction of such an embedding will form an interesting subject for further study.

Acknowledgements We like to acknowledge the support of the Netherlands Center for Earth System Science (NESSC) funded by the Netherlands Foundation for Scientific Research (NWO). This work was carried out on the Dutch national e-infrastructure with the support of SURF Cooperative under the project SH284.

[1] J. C. Zachos, M. Pagani, L. Sloan, E. Thomas, K. Billups, Trends, rythms, and aberrations in global climate 65 Ma to present, Science 292 (2001a) 686–693.

[2] J. C. Zachos, L. R. Kump, Carbon cycle feedbacks and the initiation of Antarctic glaciation in the earliest Oligocene, Global and Planetary Change 47 (1) (2005) 51–66. doi:10.1016/j.gloplacha.2005.01.001.

[3] R. M. DeConto, D. Pollard, P. A. Wilson, H. Pälike, C. H. Lear, M. Pagani, Thresholds for Cenozoic bipolar glaciation, Nature 455 (7213) (2008) 652–656. doi:10.1038/nature07337.
URL http://www.nature.com/doifinder/10.1038/nature07337

[4] H. K. Coxall, P. a. Wilson, H. Pälike, C. H. Lear, J. Backman, Rapid stepwise onset of Antarctic glaciation and deeper calcite compensation in the Pacific Ocean., Nature 433 (7021) (2005) 53–57. doi:10.1038/nature03135.

[5] M. Tigchelaar, A. S. Von Der Heydt, H. A. Dijkstra, A new mechanism for the two-step ??18O signal at the eocene-oligocene boundary, Climate of the Past 7 (1) (2011) 235–247. doi:10.5194/cp-7-235-2011.

[6] H. Stommel, Thermohaline convection with two stable regimes of flow, Tellus 2 (1961) 244–230.

[7] D. J. Lunt, M. Huber, E. Anagnostou, M. L. J. Baatsen, R. Caballero, R. DeConto, H. A. Dijkstra, Y. Donnadieu, D. Evans, R. Feng, G. L. Foster, E. Gasson, A. S. von der Heydt, C. J. Hollis, G. N. Inglis, S. M. Jones, J. Kiehl, S. Kirtland Turner, R. L. Korty, R. Kozdon, S. Krishnan, J.-B. Ladant, P. Langebroek, C. H. Lear, A. N. LeGrande, K. Littler, P. Markwick, B. Otto-Bliesner, P. Pearson, C. J. Poulsen, U. Salzmann, C. Shields, K. Snell, M. Stärz, J. Super, C. Tabor, J. E. Tierney, G. J. L. Tourte, A. Tripati, G. R. Upchurch, B. S. Wade, S. L. Wing, A. M. E. Winguth, N. M. Wright, J. C. Zachos, R. E. Zeebe, The DeepMIP contribution to PMIP4: experimental design for model simulations of the EECO, PETM, and pre-PETM (version 1.0), Geoscientific Model Development 10 (2) (2017) 889–901. doi:10.5194/gmd-10-889-2017.
URL http://www.geosci-model-dev.net/10/889/2017/

[8] H. B. Keller, Numerical solution of bifurcation and nonlinear eigenvalue problems, in: Applications of bifurcation theory (Proc. Advanced Sem., Univ. Wisconsin, Madison, Wis., 1976), Academic Press, New York, 1977, pp. 359–384. Publ. Math. Res. Center, No. 38.

[9] H. A. Dijkstra, F. W. Wubs, A. K. Cliffe, E. Doedel, I. F. Dragomirescu, B. Eckhardt, A. Y. Gelfgat, A. L. Hazel, V. Lucarini, A. G. Salinger, E. T. Phipps, J. Sanchez-Umbria, H. Schuttelaars, L. S. Tuckerman, U. Thiele, Numerical Bifurcation Methods and their Application to Fluid Dynamics: Analysis beyond Simulation, Communications in Computational Physics 15 (01) (2015) 1–45.

[10] F. W. Primeau, Multiple equilibria and low-frequency variability of the wind-driven ocean circulation, jpo 32 (2002) 2236–2256.

[11] E. Simonnet, M. Ghil, H. A. Dijkstra, Homoclinic bifurcations of barotropic qg double-gyre flows, jmr 63 (2005) 931–956.

[12] H. A. Dijkstra, Nonlinear Physical Oceanography, Vol. 28, Springer, 2005. doi:10.1007/1-4020-2263-8.
URL http://link.springer.com/10.1007/1-4020-2263-8

[13] A. de Niet, F. Wubs, A. Terwisscha van Scheltinga, H. A. Dijkstra, A tailored solver for bifurcation analysis of ocean-climate models, Journal of Computational Physics 227 (2007) 654–679. doi:10.1016/j.jcp.2007.08.006.

[14] J. Thies, F. Wubs, H. A. Dijkstra, Bifurcation analysis of 3D ocean flows using a parallel fully-implicit ocean model, Ocean Modelling 30 (4) (2009) 287–297. doi:10.1016/j.ocemod.2009.07.005.
URL http://dx.doi.org/10.1016/j.ocemod.2009.07.005

[15] E. Bernsen, H. A. Dijkstra, F. W. Wubs, Bifurcation analysis of wind-driven flows with MOM4, Ocean Modelling 30 (2-3) (2009) 95–105.

[16] S. Khatiwala, M. Visbeck, M. A. Cane, Accelerated simulation of passive tracers in ocean circulation models, Ocean Modelling 9 (2005) 51–69.

[17] E. Bernsen, H. A. Dijkstra, F. W. Wubs, A method to reduce the spin-up time of ocean models, Ocean Modelling 20 (2008) 380–392.

[18] T. M. Merlis, S. Khatiwala, Fast dynamical spin-up of ocean general circulation models using newton-krylov methods, Ocean Modelling 21 (2008) 97–105.

[19] A. W. Omta, H. A. Dijkstra, A physical mechanism for the Atlantic-Pacific flow reversal in the early Miocene, Global and Planetary Change 36 (4) (2003) 265–276. doi:10.1016/S0921-8181(02)00221-7.

[20] M. Baatsen, D. J. J. van Hinsbergen, A. S. von der Heydt, H. A. Dijkstra, A. Sluijs, H. A. Abels, P. K. Bijl, Reconstructing geographical boundary conditions for palaeoclimate modelling during the Cenozoic, Climate Of The Past 12 (8) (2016) 1635–1644.

[21] E. Bernsen, H. A. Dijkstra, J. Thies, F. W. Wubs, The application of Jacobian-free Newton-Krylov methods to reduce the spin-up time of ocean general circulation models, Journal of Computational Physics 229 (21) (2010) 8167–8179. doi:10.1016/j.jcp.2010.07.015.
URL http://dx.doi.org/10.1016/j.jcp.2010.07.015

[22] R. Seydel, Practical Bifurcation and Stability Analysis, Vol. 5 of Interdisciplinary Applied Mathematics, Springer New York, New York, NY, 2010. doi:10.1007/978-1-4419-1740-9.
URL http://link.springer.com/10.1007/978-1-4419-1740-9

[23] J. E. Dennis, Jr, R. B. Schnabel, Numerical Methods for Unconstrained Optimization and Nonlinear Equations, SIAM Classics in Applied Mathematics, SIAM, 1996.

[24] F. Bryan, Parameter Sensitivity of Primitive Equation Ocean General Circulation Models (1987). doi:10.1175/1520-0485(1987)017<0970:PSOPEO>2.0.CO;2.
URL http://dx.doi.org/10.1175/1520-0485(1987)017<0970:PSOPEO>2.0.CO\nhttp://jour

[25] T. H. Torsvik, R. Van der Voo, U. Preeden, C. M. Niocaill, B. Steinberger, P. V. Doubrovine, D. J. J. van Hinsbergen, M. Domeier, C. Gaina, E. Tohver, J. G. Meert, P. J. A. McCausland, L. R. M. Cocks, Phanerozoic polar wander, palaeogeography and dynamics, Earth-Science Reviews 114 (3-4) (2012) 325–368. doi:10.1016/j.earscirev.2012.06.002.

[26] D. J. J. van Hinsbergen, L. V. de Groot, S. J. van Schaik, W. Spakman, P. K. Bijl, A. Sluijs, C. G. Langereis, H. Brinkhuis, A Paleolatitude Calculator for Paleoclimate Studies., PloS one 10 (6) (2015) e0126946. doi:10.1371/journal.pone.0126946.
URL http://journals.plos.org/plosone/article?id=10.1371/journal.pone.0126946

[27] R. D. Müller, M. Sdrolias, C. Gaina, W. R. Roest, Age, spreading rates, and spreading asymmetry of the world's ocean crust, Geochemistry, Geophysics, Geosystems 9 (4). doi:10.1029/2007GC001743.

[28] A. von der Heydt, H. A. Dijkstra, Effect of ocean gateways on the global ocean circulation in the late Oligocene and early Miocene, Paleoceanography 21 (2006) PA1011. doi:10.1029/2005PA001149.

[29] Y. Saad, A Flexible Inner-Outer Preconditioned GMRES Algorithm, SIAM Journal on Scientific Computing 14 (2) (1993) 461–469. doi:10.1137/0914028.
URL http://epubs.siam.org/doi/abs/10.1137/0914028

[30] I. Gruais, N. M. M. Cousin-Rittemard, H. A. Dijkstra, A priori estimations of a global homotopy residue continuation method, Numerical Functional Analysis and Optimization 26 (4-5) (2005) 507–521. doi:10.1080/01630560500248306.

[31] A. von der Heydt, H. A. Dijkstra, Flow reorganizations in the panama seaway: A cause for the demise of miocene corals?, Geophysical Research Letters 32 (2) (2005) n/a–n/a, l02609.

[32] S. E. Huisman, H. A. Dijkstra, A. S. von der Heydt, W. P. M. de Ruijter, Does net E−P set a preference for north atlantic sinking?, Journal of Physical Oceanography 42 (11) (2012) 1781–1792.

[33] J. Sánchez, M. Net, B. García-Archilla, C. Simó, Newton-krylov continuation of periodic orbits for navier-stokes flows, Journal of Computational Physics 201 (1) (2004) 13–33. doi:10.1016/j.jcp.2004.04.018.
URL http://www.sciencedirect.com/science/article/pii/S0021999104001895